

REPORT DOCUMENTATION PAGE

Form Approved
OMB No. 0704-0188

The public reporting burden for this collection of information is estimated to average 1 hour per response, including the time for reviewing instructions, searching existing data sources, gathering and maintaining the data needed, and completing and reviewing the collection of information. Send comments regarding this burden estimate or any other aspect of this collection of information, including suggestions for reducing the burden, to the Department of Defense, Executive Service Directorate (0704-0188). Respondents should be aware that notwithstanding any other provision of law, no person shall be subject to any penalty for failing to comply with a collection of information if it does not display a currently valid OMB control number.

PLEASE DO NOT RETURN YOUR FORM TO THE ABOVE ORGANIZATION.

1. REPORT DATE (DD-MM-YYYY) 02-25-2010		2. REPORT TYPE Final	3. DATES COVERED (From - To) 1 Mar 2007-30 Nov 2009	
4. TITLE AND SUBTITLE Realization of Metamaterial-Based Devices: Mathematical theory and Physical demonstration			5a. CONTRACT NUMBER FA9550-07-1-0133	
			5b. GRANT NUMBER	
			5c. PROGRAM ELEMENT NUMBER	
			5d. PROJECT NUMBER	
			5e. TASK NUMBER	
6. AUTHOR(S) Hossein Mosallaei			5f. WORK UNIT NUMBER	
7. PERFORMING ORGANIZATION NAME(S) AND ADDRESS(ES) Northeastern University 360 Huntington Avenue Boston, MA 02115			8. PERFORMING ORGANIZATION REPORT NUMBER	
9. SPONSORING/MONITORING AGENCY NAME(S) AND ADDRESS(ES) Air Force Office of Scientific Research 875 North Randolph Street Suite 325, Rm 3112 Arlington, VA 22203			10. SPONSOR/MONITOR'S ACRONYM(S) AFOSR	
			11. SPONSOR/MONITOR'S REPORT NUMBER(S) AFRL-SR-AR-TR-10-0097	

12. DISTRIBUTION/AVAILABILITY STATEMENT
Distribution A: Approved for Public Release

20100316241

13. SUPPLEMENTARY NOTES

14. ABSTRACT

The focus of this project was on dipole mode analysis and dispersion diagram characteristics of metamaterials constructed from array of dielectric and magnetic spheres in a unit-cell. A comprehensive study was provided and different metamaterials were established. It was demonstrated combining electric and magnetic dipole modes (different spheres particles in a unit-cell) can successfully engineer the dispersion diagrams. Effective metamaterials parameters were obtained. Bandwidth enhancement by increasing the coupling between the particles was also realized. The performance analysis of other shape structures (such as disks, casier for fabrication) was also explored. At the end, hemisphere magneto-dielectric, ENG, and MNG small antennas were developed and their physics were highlighted. Our theoretical model was successfully validated using a full-wave numerical approach through successful modeling of complex metamaterial structures.

15. SUBJECT TERMS

Metamaterials, Dipole-Modes, Dispersion Diagram, Array of Spheres, Magneto-Dielectric Particles

16. SECURITY CLASSIFICATION OF:			17. LIMITATION OF ABSTRACT SAR	18. NUMBER OF PAGES 22	19a. NAME OF RESPONSIBLE PERSON Dr. Hossein Mosallaei
a. REPORT U	b. ABSTRACT U	c. THIS PAGE U			19b. TELEPHONE NUMBER (Include area code)

Realization of Metamaterial-Based Devices: Mathematical Theory and Physical Demonstration

Final Report

Mar 2007-Nov 2009

Air Force Office of Scientific Research (AFOSR)

ATTN: Dr. Arje Nachman
875 North Randolph Road
Ste 325, Room 3112
Arlington, VA 22203
Phone: (703) 696-8427

Fax: (703) 696-8450, Email: arje.nachman@afosr.af.mil

Technical Point of Contact

Professor Hossein Mosallaei (Principal Investigator)
Northeastern University
360 Huntington Avenue
Boston, MA 02115
Phone: (617) 373-7354
Fax: (617) 373-8970, Email: hosseinm@ece.neu.edu

Administrative Point of Contact

Deborah Grupp-Patruz, Director
Office of Research Administration and Finance
Northeastern University
960 Renaissance Park
360 Huntington Avenue
Boston, MA 02115
Phone: (617) 373-5600, Fax: (617) 373-4595
Email: DSPA@neu.edu

2/25/2010

Realization of Metamaterial-Based Devices: Mathematical theory and Physical Demonstration

Hossein Mosallaei
ECE Department
Northeastern University
Email: hosseinm@ece.neu.edu

This project focuses on dipole mode analysis and dispersion diagram characteristics of metamaterials constructed from array of dielectric and magnetic spheres in a unit-cell. A comprehensive study is provided and different metamaterials are established. It is demonstrated combining electric and magnetic dipole modes (different spheres particles in a unit-cell) can successfully engineer the dispersion diagrams. Effective metamaterials parameters are obtained. Bandwidth enhancement by increasing the coupling between the particles is also realized. The performance analysis of other shape structures (such as disks, easier for fabrication) is also explored. At the end, hemisphere magneto-dielectric, ENG, and MNG small antennas are developed and their physics are highlighted. Our theoretical model is successfully validated using a full-wave numerical approach through successful modeling of complex metamaterial structures. It must be mentioned that in this report a detailed-summary is presented, where the full and comprehensive discussions can be found in published papers and dissertation made in-part out of this work (see references). One student has been fully working on this project (however some of my other students have also helped with discussions and some simulations)

1. Array of Spheres

Modeling of array of dielectric spheres (see Fig. 1), with arbitrary geometries and locations, are explored. The incoming and scattered fields for each sphere is expressed in terms of Mie-series as below [1]

$$\mathbf{E}_p^i = \sum_{n=1}^{\infty} \sum_{m=-n}^n [A_{mn}^{ip} \mathbf{N}_{mn}^{(1)}(r_p, \theta_p, \phi_p) + B_{mn}^{ip} \mathbf{M}_{mn}^{(1)}(r_p, \theta_p, \phi_p)] \quad (1a)$$

$$\eta \mathbf{H}_p^i = -j \sum_{n=1}^{\infty} \sum_{m=-n}^n [A_{mn}^{ip} \mathbf{M}_{mn}^{(1)}(r_p, \theta_p, \phi_p) + B_{mn}^{ip} \mathbf{N}_{mn}^{(1)}(r_p, \theta_p, \phi_p)] \quad (1b)$$

$$\mathbf{E}_p^s = \sum_{n=1}^{\infty} \sum_{m=-n}^n [A_{mn}^{sp} \mathbf{N}_{mn}^{(3)}(r_p, \theta_p, \phi_p) + B_{mn}^{sp} \mathbf{M}_{mn}^{(3)}(r_p, \theta_p, \phi_p)] \quad (2a)$$

$$\eta \mathbf{H}_p^s = -j \sum_{n=1}^{\infty} \sum_{m=-n}^n [A_{mn}^{sp} \mathbf{M}_{mn}^{(3)}(r_p, \theta_p, \phi_p) + B_{mn}^{sp} \mathbf{N}_{mn}^{(3)}(r_p, \theta_p, \phi_p)] \quad (2b)$$

And then using the additional theorems and applying the boundary conditions the required unknown parameters are derived:

$$A_{mn}^{sp} = \zeta_n(a) (A_{mn}^{ip} + \sum_{q \neq p} \sum_{v=1}^{\infty} \sum_{\mu=-v}^v [A_{mn\mu v} (d_{pq}, \theta_{pq}, \phi_{pq}) A_{\mu v}^{sq} + B_{mn\mu v} (d_{pq}, \theta_{pq}, \phi_{pq}) B_{\mu v}^{sq}]), \quad (3a)$$

$$B_{mn}^{sp} = \xi_n(a) (B_{mn}^{ip} + \sum_{q \neq p} \sum_{v=1}^{\infty} \sum_{\mu=-v}^v [A_{mn\mu v} (d_{pq}, \theta_{pq}, \phi_{pq}) B_{\mu v}^{sq} + B_{mn\mu v} (d_{pq}, \theta_{pq}, \phi_{pq}) A_{\mu v}^{sq}]). \quad (3b)$$

Where the summation over q is the summation on all particles except the reference sphere. d_{pq} is the center distance between p^{th} sphere and q^{th} one. $A_{mn}^{\mu v}$ and $B_{mn}^{\mu v}$ are the translational addition theorem coefficients. Equations (3) are a coupled set of complex linear algebraic equations, and

should be solved simultaneously to yield the unknown scattering coefficients. In addition, the infinite series must be truncated to a finite number $n = \nu = N$ and $m = \mu = M$. To obtain the scattering coefficient first we have to determine the vector translation additional coefficients. Based on the Cruzan's theorem, the translation addition coefficients are [2]:

$$A_{mn\mu\nu}(d, \theta, \phi) = (-1)^m e^{i(\mu-m)\phi} \sum_p a(-m, n, \mu, \nu, p) a(n, \nu, p) h_p^{(1)}(kd) P_p^{\mu-m}(\cos \theta) \quad (4a)$$

$$B_{mn\mu\nu}(d, \theta, \phi) = (-1)^{m+1} e^{i(\mu-m)\phi} \sum_p a(-m, n, \mu, \nu, p, p-1) b(n, \nu, p) h_p^{(1)}(kd) P_p^{\mu-m}(\cos \theta) \quad (4b)$$

In the above equations $h_p^{(1)}$ represents the Hankel function of the first kind, P_n^m is the associated Legendre function of the first kind. The $a(-m, n, \mu, \nu, p)$ and $a(-m, n, \mu, \nu, p, p-1)$ are the Gaunt coefficients [3]. The Gaunt coefficient are closely related to Wigner 3jm symbol and defined by:

$$a(-m, n, \mu, \nu, p) = (-1)^{(\mu-m)} (2p+1) \left[\frac{(n-m)!(\nu+\mu)!(p+m-\mu)!}{(n+m)!(\nu-\mu)!(p-m+\mu)!} \right]^{1/2} \begin{pmatrix} n & \nu & p \\ 0 & 0 & 0 \end{pmatrix} \begin{pmatrix} n & \nu & p \\ -m & \mu & m-\mu \end{pmatrix} \quad (5a)$$

$$a(-m, n, \mu, \nu, p, p-1) = (-1)^{(\mu-m)} (2p+1) \left[\frac{(n-m)!(\nu+\mu)!(p+m-\mu)!}{(n+m)!(\nu-\mu)!(p-m+\mu)!} \right]^{1/2} \begin{pmatrix} n & \nu & p \\ 0 & 0 & 0 \end{pmatrix} \begin{pmatrix} n & \nu & p-1 \\ -m & \mu & m-\mu \end{pmatrix} \quad (5b)$$

The other coefficients in (3) are defined as:

$$a(n, \nu, p) = \frac{j^{(n-\nu+p)}}{2n(n+1)} \quad (6a)$$

$$b(n, \nu, p) = \frac{j^{(n-\nu+p)} (2n+1)}{2n(n+1)} ((n+\nu+p+1)(n+p-\nu)(\nu+p-n)(n+\nu-p+1))^{1/2} \quad (6b)$$

Note that, the integer p in the summation of (3a) takes the values of $|n-\nu|, |n-\nu|+2, \dots, n+\nu$. While this integer (p) in (3b) varies from $|n-\nu|+1, |n-\nu|+3, \dots, n+\nu$. The Wigner 3jm symbol is defined as:

$$\begin{pmatrix} j1 & j2 & j3 \\ m1 & m2 & m3 \end{pmatrix} = (-1)^{j1+j2+m3} \times \left[\frac{(j1-m1)!(j1+m1)!(j2-m2)!(j2+m2)!(j3-m3)!(j3+m3)!}{(j1+j2-j3)!(j1-j2+j3)!(-j1+j2+j3)!(j1+j2+j3+1)!} \right]^{1/2} \times \sum_{k=k_{min}}^{k_{max}} (-1)^k \begin{pmatrix} j1+j2-j3 \\ k \end{pmatrix} \begin{pmatrix} j1-j2+j3 \\ j1-m1-k \end{pmatrix} \begin{pmatrix} -j1+j2+j3 \\ j2+m2-k \end{pmatrix} \quad (7)$$

Once we calculated all the addition theorems, the scattering coefficients can be calculated using (3). Now that we have the scattering coefficients, the total scattering field of the entire cluster can be obtained. In the far-field region the relation between the electric vector components of the incident field and those of the scattered filed is given by:

$$E \parallel_s = \frac{e^{ikr}}{-ikr} (S_2 E \parallel_i + S3 E \perp_i) \quad (8a)$$

$$E \perp_s = \frac{e^{ikr}}{-ikr} (S_4 E \parallel_i + S1 E \perp_i) \quad (8b)$$

where k is the wave number and r is the usual spherical coordinate for a point in space. The electric vector components $(E \parallel_i, E \perp_i)$ and $(E \parallel_s, E \perp_s)$ of the incident and scattered fields are parallel and perpendicular respectively to the scattering plane defined by the direction of the incident wave vector and the scattering direction. To check the accuracy of the scattering coefficient, we compare the theoretical results of components of polarized scattered intensity i_{11} and i_{22} with the experimental results in [4, 5]. i_{11} and i_{22} are functions of the scattering angle θ alone, when referred to the scattering plane only ($\phi=0$) and can be calculated from the amplitude scattering matrix through the equations

$$i_{11} = |S_1^y(\theta)|^2 \quad (9a)$$

$$i_{22} = |S_2^x(\theta)|^2 \quad (9b)$$

where the superscript x or y indicates that the incident plane wave is x or y polarized (note that the incident plane wave propagates along the z axis). For each sphere, S_1^y and S_1^x are defined as follows:

$$S_1^y(\theta) = \sum_{p=1}^N e^{-ik \cdot d_p} \sum_{n=1}^{\infty} \sum_{m=-n}^n A_{mn}^{sp} \frac{m}{\sin \theta} P_n^m(\cos \theta) + B_{mn}^{sp} \frac{d}{d\theta} P_n^m(\cos \theta) \quad (10a)$$

$$S_2^x(\theta) = \sum_{p=1}^N e^{-ik \cdot d_p} \sum_{n=1}^{\infty} \sum_{m=-n}^n B_{mn}^{sp} \frac{m}{\sin \theta} P_n^m(\cos \theta) + A_{mn}^{sp} \frac{d}{d\theta} P_n^m(\cos \theta) \quad (10b)$$

The scattering parameters for two types of structures are obtained in Figs. 2 and 3. The results are compared very successfully with experimental demonstrations in [4, 5], validating the accuracy of our technique. Note that, for all the cases, the axis of symmetry of each sphere chain is perpendicular to either the scattering plane x-z plane or the incident wave vector along the z axis. In other words, it is always parallel to the y axis.

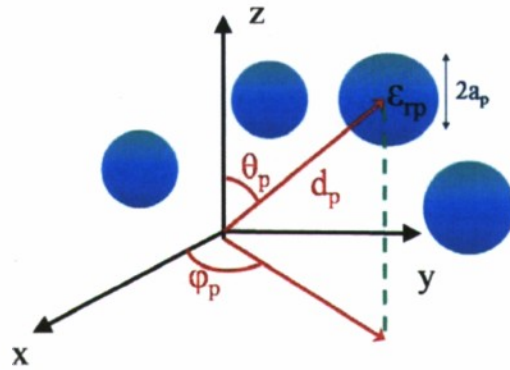


Fig. 1: Configuration of an aggregate of spheres.

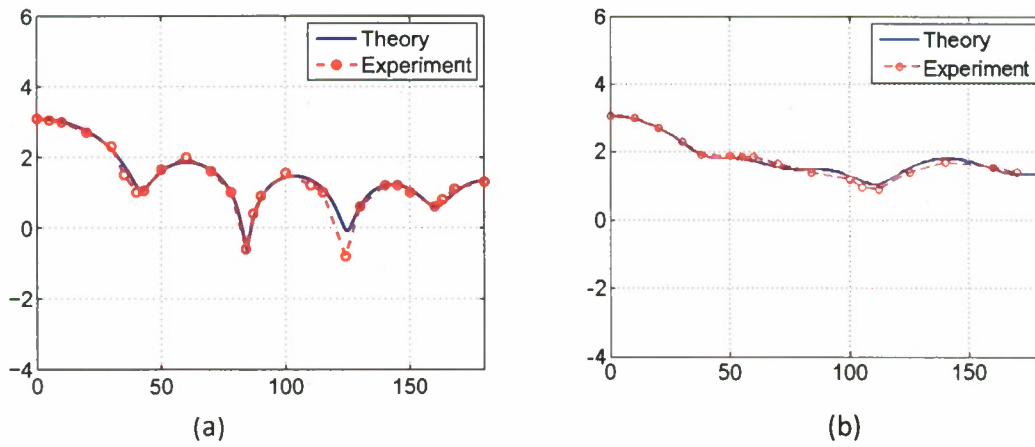


Fig. 2: Comparison of theoretical calculations with laboratory scattering measurements from [5] for angular distributions of polarization components of scattered intensity by two identical spheres with inter-sphere distance of 10.76. Each sphere has a size parameter of $ka=4.346$ and a refractive index of $\epsilon_r=2.6568 + 0.0326i$, $\mu_r=1$ (a) $\log(i11)$, (b) $\log(i22)$.

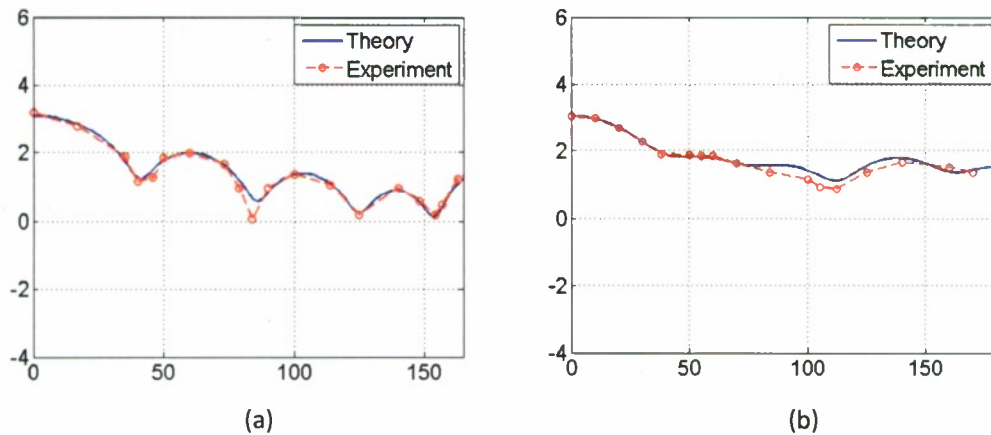


Fig. 3: Comparison of theoretical calculations with laboratory scattering measurements from [5] for angular distributions of polarization components of scattered intensity by two identical spheres with inter-sphere distance of 9.94. Each sphere has a size parameter of $ka=4.346$ and a refractive index of $\epsilon_r=2.6568+0.0326i$, $\mu_r=1$ (a) $\log(i11)$, (b) $\log(i22)$.

2. Two-Set Dielectric Spheres Unit-Cell

The objective in this section is to investigate metamaterials constructed from arrays of two-set of spheres in a unit cell, as illustrated in Fig. 4. Considering one is exploring a metamaterial realization, the spheres sizes must be subwavelength and thus one can use the equations derived in section 1 and simplify them by considering only the electric and magnetic dipole modes. This will extensively reduce the complexity of the modeling. Figs. 5(a) and 5(b) demonstrate the scattering performance of a single sphere around the frequency band that only the electric and magnetic modes exist. As one can see the scattering coefficients goes to resonance but at different frequencies. To achieve a metamaterial with tailored electric and magnetic parameters, one needs to bring these two resonances around the same spectrum. This can simply be achieved by making a metamaterial constructed from two spheres in a unit cell (the same materials and different sizes or the same sizes and different materials).

The structure is a complex configuration and one needs to comprehensively model the metamaterial. A reciprocity technique is applied that the fields on a reference sphere is equal to the scattered fields from all other spheres at that element. Using the periodic boundary condition and the fact that a travelling wave with proper phase shift exists through the array, the below equation for achieving the dispersion diagram for metamaterial ($kd-\beta d$) is achieved [1, 6]:

$$\frac{b'_{-0}}{S'_-} = b'_{-0} \sum_{ee_{\tau\tau}} + b'_{-0} \sum_{ee_{\tau\tau}} - b'_{+0} \sum_{eh_{\tau\tau}} - b'_{+0} \sum_{eh_{\tau\tau}} \quad (11a)$$

$$\frac{b'_{+0}}{S'_+} = -b'_{-0} \sum_{he_{\tau\tau}} - b'_{-0} \sum_{he_{\tau\tau}} + b'_{+0} \sum_{hh_{\tau\tau}} + b'_{+0} \sum_{hh_{\tau\tau}} \quad (11b)$$

S'_- and S'_+ for $\iota \in \{1,2\}$ are the normalized Mie electric and magnetic scattering coefficients,

$$S_- = \frac{3j}{2} \zeta_1(a) \quad (12a)$$

$$S_+ = \frac{3j}{2} \xi_1(a) \quad (12b)$$

$\zeta_1(a)$ and $\xi_1(a)$ are the first Mie electric and magnetic scattering coefficient:

$$\zeta_n(a) = -\frac{\mu_r j_n(ka)(k_p a j_n(k_p a))' - \mu_r \epsilon_r j_n(k_p a)(k a j_n(ka))'}{\mu_r h_n^{(2)}(ka)(k_p a j_n(k_p a))' - \mu_r \epsilon_r j_n(k_p a)(k a h_n^{(2)}(ka))'} \quad (13a)$$

$$\xi_n(a) = -\frac{\mu_r j_n(k_p a)(k a j_n(ka))' - \mu_r j_n(ka)(k_p a j_n(k_p a))'}{\mu_r j_n(k_p a)(k a h_n^{(2)}(ka))' - \mu_r h_n^{(2)}(ka)(k_p a j_n(k_p a))'} \quad (13b)$$

Here k_p is the wavenumber inside the p^{th} sphere while j_n and $h_n^{(2)}$ are the spherical Bessel and spherical Hankel function of the second kind. The summations defined in (11) are given by [6]:

$$\Sigma_{eeii} = \sum_{l_z=-\infty}^{\infty} e^{-jl_z \beta d} \sum_{\substack{l_x=-\infty \\ (l_x, l_y, l_z) \neq (0,0,0)}}^{\infty} \sum_{l_y=-\infty}^{\infty} \frac{e^{-jkr_{l_x l_y l_z}^{ii}}}{kr_{l_x l_y l_z}^{ii}}$$

$$\left[\frac{2j}{kr_{l_x l_y l_z}^{ii}} \left(1 + \frac{-j}{kr_{l_x l_y l_z}^{ii}} \right) \frac{(l_x h_x)^2}{(r_{l_x l_y l_z}^{ii})^2} + \left(1 + \frac{-j}{kr_{l_x l_y l_z}^{ii}} - \frac{1}{(kr_{l_x l_y l_z}^{ii})^2} \right) \frac{(l_y h_y)^2 + (l_z d)^2}{(r_{l_x l_y l_z}^{ii})^2} \right] \quad (14a)$$

$$\Sigma_{eetri} = \sum_{l_z=-\infty}^{\infty} e^{-jl_z \beta d} \sum_{l_x=-\infty}^{\infty} \sum_{l_y=-\infty}^{\infty} \frac{e^{-jkr_{l_x l_y l_z}^{ti}}}{kr_{l_x l_y l_z}^{ti}}$$

$$\left[\frac{2j}{kr_{l_x l_y l_z}^{ti}} \left(1 + \frac{-j}{kr_{l_x l_y l_z}^{ti}} \right) \frac{(l_x h_x + h)^2}{(r_{l_x l_y l_z}^{ti})^2} + \left(1 + \frac{-j}{kr_{l_x l_y l_z}^{ti}} - \frac{1}{(kr_{l_x l_y l_z}^{ti})^2} \right) \frac{(l_y h_y)^2 + (l_z d)^2}{(r_{l_x l_y l_z}^{ti})^2} \right] \quad (14b)$$

$$\Sigma_{hhii} = \sum_{l_z=-\infty}^{\infty} e^{-jl_z \beta d} \sum_{\substack{l_x=-\infty \\ (l_x, l_y, l_z) \neq (0,0,0)}}^{\infty} \sum_{l_y=-\infty}^{\infty} \frac{e^{-jkr_{l_x l_y l_z}^{ii}}}{kr_{l_x l_y l_z}^{ii}}$$

$$\left[\frac{2j}{kr_{l_x l_y l_z}^{ii}} \left(1 + \frac{-j}{kr_{l_x l_y l_z}^{ii}} \right) \frac{(l_y h_y)^2}{(r_{l_x l_y l_z}^{ii})^2} + \left(1 + \frac{-j}{kr_{l_x l_y l_z}^{ii}} - \frac{1}{(kr_{l_x l_y l_z}^{ii})^2} \right) \frac{(l_x h_x)^2 + (l_z d)^2}{(r_{l_x l_y l_z}^{ii})^2} \right] \quad (14c)$$

$$\Sigma_{hhtri} = \sum_{l_z=-\infty}^{\infty} e^{-jl_z \beta d} \sum_{l_x=-\infty}^{\infty} \sum_{l_y=-\infty}^{\infty} \frac{e^{-jkr_{l_x l_y l_z}^{ti}}}{kr_{l_x l_y l_z}^{ti}}$$

$$\left[\frac{2j}{kr_{l_x l_y l_z}^{ti}} \left(1 + \frac{-j}{kr_{l_x l_y l_z}^{ti}} \right) \frac{(l_y h_y)^2}{(r_{l_x l_y l_z}^{ti})^2} + \left(1 + \frac{-j}{kr_{l_x l_y l_z}^{ti}} - \frac{1}{(kr_{l_x l_y l_z}^{ti})^2} \right) \frac{(l_x h_x + h)^2 + (l_z d)^2}{(r_{l_x l_y l_z}^{ti})^2} \right] \quad (14d)$$

$$\Sigma_{ehii} = \Sigma_{heii} = \sum_{\substack{l_z=-\infty \\ n=0}}^{\infty} e^{-jl_z \beta d} \sum_{l_x=-\infty}^{\infty} \sum_{l_y=-\infty}^{\infty} \frac{e^{-jkr_{l_x l_y l_z}^{ii}}}{kr_{l_x l_y l_z}^{ii}} \left(1 + \frac{-j}{kr_{l_x l_y l_z}^{ii}} \right) \frac{l_z d}{r_{l_x l_y l_z}^{ii}} \quad (15a)$$

$$\Sigma_{ehir} = \Sigma_{heir} = \sum_{l_z=-\infty}^{\infty} e^{-jl_z \beta d} \sum_{l_x=-\infty}^{\infty} \sum_{l_y=-\infty}^{\infty} \frac{e^{-jkr_{l_x l_y l_z}^{ti}}}{kr_{l_x l_y l_z}^{ti}} \left(1 + \frac{-j}{kr_{l_x l_y l_z}^{ti}} \right) \frac{l_z d}{r_{l_x l_y l_z}^{ti}} \quad (15b)$$

It is worth noticing that, the summations in (14) are the interactions between the scattered electric (magnetic) field from other spheres and the electric (magnetic) field of reference spheres while the terms in (15) are the coupling between the scattered electric (magnetic) field from other spheres and the magnetic (electric) field of reference spheres. Also, one can divide each of the series in (14), and

(15) into two parts, one the contributions from the self plane spheres ($l_z=0$) and other the contribution from all others. For instance, Σ_{ee11} can be expressed as:

$$\Sigma_{ee11} = \Sigma_{ee11}^s + \Sigma_{ee11}^o \quad (16)$$

Where Σ_{ee11}^s is the summation over the scattered field from spheres in the self-plane (the plane of the reference sphere) and Σ_{ee11}^o is the summation of the scattered field over all other planes except $l_z=0$. These expressions help us better understand, which part provides more contribution to calculation of the $kd-\beta d$ diagram.

Since in (11), ι takes the values of 1 and 2, we have a set of four homogenous equations to be solved for deriving the desired $kd-\beta d$ relation. The dispersion relation is then obtained equating the determinant of the coefficients to zero (note that the variables are $b_{-0}^1, b_{-0}^2, b_{+0}^1$ and b_{+0}^2). It is worth mentioning that, the series in (14, 15) are slowly convergent series and hence excessive number of terms are required for the desired preciseness. Acceleration techniques have been applied to numerically solve the above transcendental equations for the propagation constant β [7, 8].

The above technique is successfully applied to metamaterials characterization. Fig. 5(c) obtains the dispersion diagram for two-set of spheres having the same size and different materials. The dispersion diagram and the existence of a negative slope branch are demonstrated. A full wave numerical technique based on Finite Difference Time Domain (FDTD) technique [9] is also applied to validate the accuracy of our developed method based on dipole-mode analysis. An excellent comparison is demonstrated, where our method is much more efficient.

An array of spheres with the unit-cells made of two different spheres (different materials and same sizes) is modeled in Fig. 6. The design is optimized such that the electric resonance of one set of spheres will be around the magnetic resonance of another set. Fig. 6(a) and 6(b) illustrate the electric and magnetic band-gaps (for each set) associated with the relevant resonances. Combining these two sets of spheres demonstrates a pass-band through the stop band region highlighting a backward metamaterial structure. One can also design a negative-slope backward wave medium utilizing different sizes spheres (having the same materials) in a unit cell, as determined in Fig. 7. It must be mentioned that the backward wave is occurred in the region that kd is larger than 1 and effective materials parameters may not be defined successfully. One can increase the dielectric materials of the spheres to bring the backward wave dispersion diagram in the region that $kd < 1$ and thus define properly the effective material parameters, as is illustrated in Fig. 8. This realizes a metamaterial with Double Negative (DNG) materials characteristics, although the bandwidth of the metamaterial is relatively small. The effect of the coupling on the dispersion diagram and its bandwidth performance is investigated in Fig. 9. This is one set of spheres operating in their magnetic resonances where their couplings provide electric modes. The hybrid modes tailor a dispersion diagram with negative slope. As one can see increasing the couplings between the elements accomplishes more bandwidth for the performance which will be a very novel idea. Full investigations and discussions about the configurations and results are provided in [6].

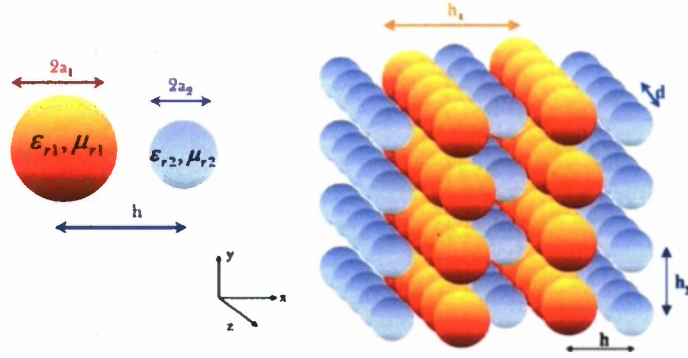


Fig. 4: Geometry of two-sets of dielectric spheres metamaterials.

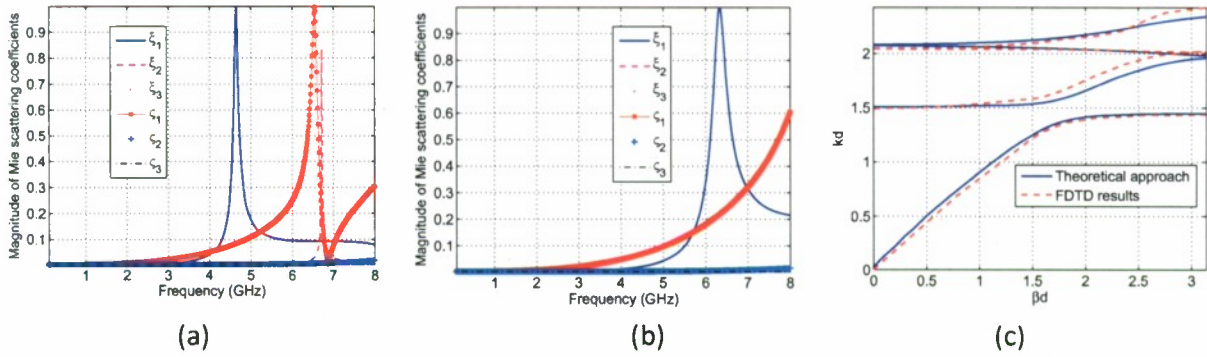


Fig. 5: Electric and magnetic Mie scattering coefficients of a single sphere for the first three modes with , (a) $a=0.5\text{cm}$ and $\epsilon_r=40$, (b) $a=0.5\text{cm}$ and $\epsilon_r=21$, (c) Comparison between FDTD results and theoretical approach for two-sets of dielectric spheres with $a_1=a_2=0.5\text{cm}$, $d/a=3$, $h_x/a=h_y/a=5$, $h=h_x/2$, $\epsilon_{r1}=40$ and $\epsilon_{r2}=21$. A very good agreement between our theoretical model and FDTD is observed.

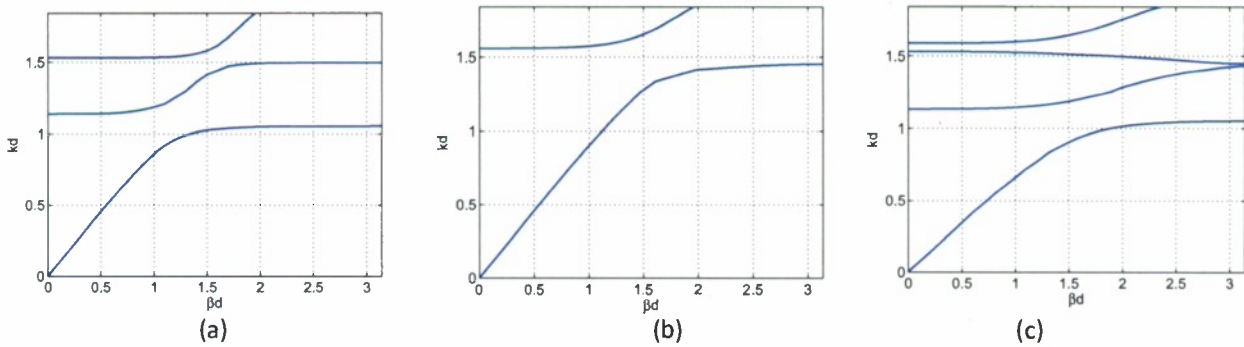


Fig. 6: Dispersion diagrams for two-sets of dielectric spheres having the same sizes ($a_1=a_2=0.5\text{cm}$) and different dielectric materials, (a) The performance of the first set described with $\epsilon_{r1}=40$ and $d=1.1\text{cm}$, $h_x=h_y=2.5\text{cm}$, (b) The performance of the second set described with $\epsilon_{r2}=20.5$, $d=1.1\text{cm}$ and $h_x=h_y=2.5\text{cm}$, (c) The performance of the combinations of the two-sets with $h=h_x/2$.

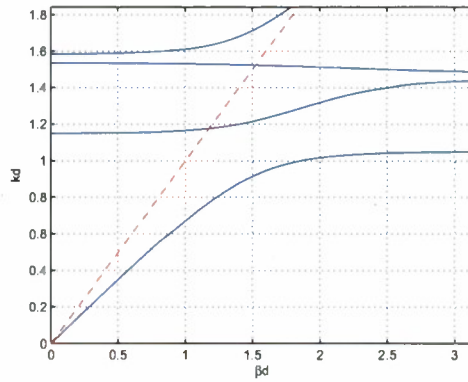


Fig. 7: Dispersion diagrams for two-sets of dielectric spheres having the same dielectric materials ($\epsilon_{r1} = \epsilon_{r2} = 40$) and different radii, $a_1 = 0.5\text{cm}$ and $a_2 = 0.356\text{cm}$, $d = 1.1\text{cm}$, $h_x = h_y = 1.8\text{cm}$, $h = h_x/2$.

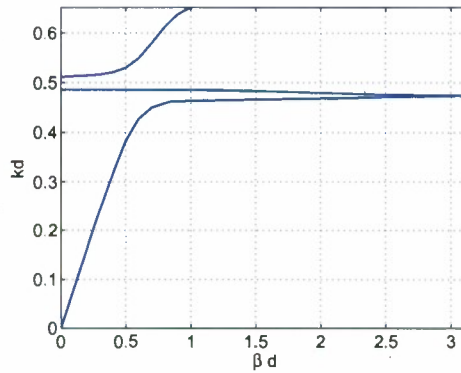


Fig. 8: Dispersion diagrams for two-sets of dielectric spheres having the same sizes and different dielectric materials $\epsilon_{r1} = 98$, $\epsilon_{r2} = 200$, $a_1 = a_2 = 0.5\text{cm}$, $d/a = 2.1$, $h_x = h_y = 2.5\text{cm}$ and $h = h_x/2$. $kd < 1$ is achieved where one can define effective materials parameters.

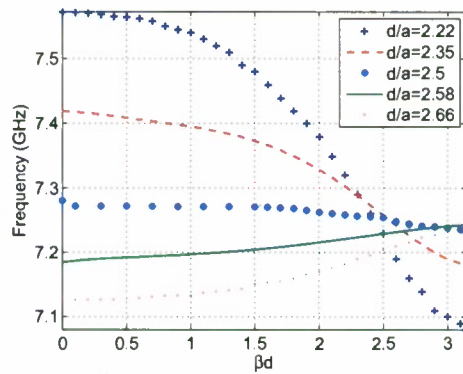


Fig. 9: Dispersion diagram characteristic for the second branch of array of highly coupled cubical unit-cell spheres having $\epsilon_r = 20$, $a = 0.5\text{cm}$ and $h_x = h_y = d$. Increasing the coupling will change the performance from positive slope to negative slope.

3. Magnetic Materials-Based Spheres Metamaterials

We also investigate the performance of metamaterials realization utilizing array of magneto-dielectric spheres or dielectric spheres embedded in a host natural hexa-ferrite medium operating in its negative permeability region [10]. The advantage of integrating magnetic materials is achieving wider bandwidth as has been explored earlier by Mosallaei in [11].

Our developed formulation is general, and Fig. 10 demonstrates the characteristics for an array of magneto-dielectric spheres [6]. The scattering coefficients and dispersion diagram are shown in Fig. 10. The scattering coefficient is for a single sphere highlighting the electric and magnetic resonances around the same frequency region. Making an array of spheres considering the couplings between them realizes a backward wave medium in the region that $kd < 1$, and where a wider bandwidth in compared to only dielectric design is established. The effective materials parameters are obtained in Fig. 11 proving a DNG medium with both negative ϵ and μ .

We also exploit a novel design of one set of array of dielectric spheres embedded in a natural hexa-ferrite material with Lorentzian property given by [10] (and plotted in Fig. 12(a))

$$\mu = \mu_0 \left(1 - \frac{\omega^2}{\omega^2 - (2\pi \times 2 \times 10^9)^2} \right) \quad (17)$$

The dielectric particles are designed to operate in their electric resonances (around the spectrum where the host material has its own negative permeability). The performance is determined in Fig. 12(b). The effective materials associated with this design are plotted in Fig. 13. In compared to previous design a better performance with more negative permeability range is developed.

The integration of magnetic materials can also allow tunability by applying magnetic DC fields.

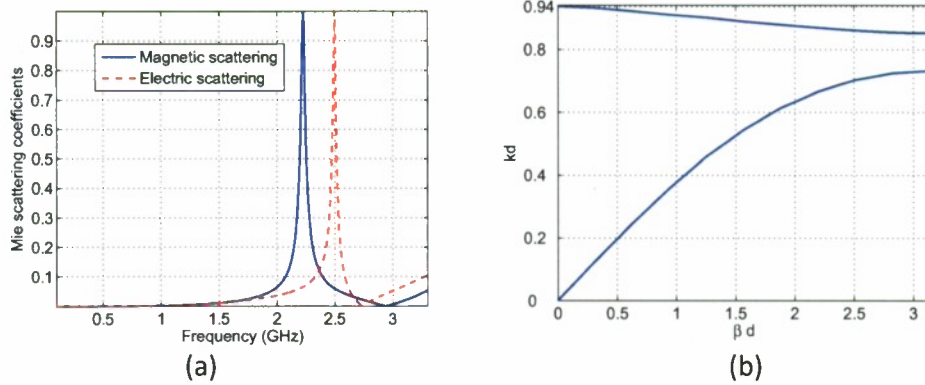


Fig. 10: (a) Mie scattering coefficients for a single magneto dielectric sphere with $\epsilon_r = 18$, $\mu_r = 5$, $a = 0.85 \text{ cm}$, (b) dispersion diagram characteristic for one-set of magneto dielectric spheres with $a = 0.85 \text{ cm}$, $d/a = 2.1$ and $h_x = h_y = d$.

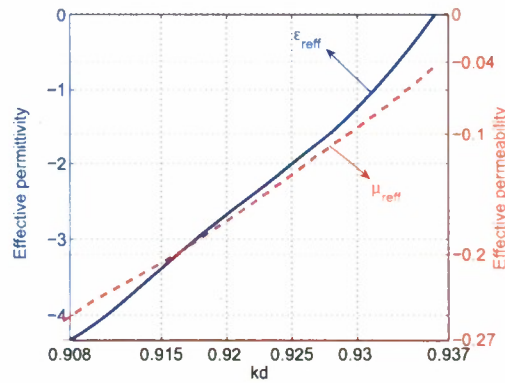


Fig. 11: Effective permittivity and permeability for 3D array of magneto-dielectric spheres with cubical unit cell and $a = 0.85 \text{ cm}$, $\epsilon_r = 18$, $\mu_r = 5$, $d/a = 2.1$. The bulk materials are plotted in the region where both $kd, \beta d < 1$.

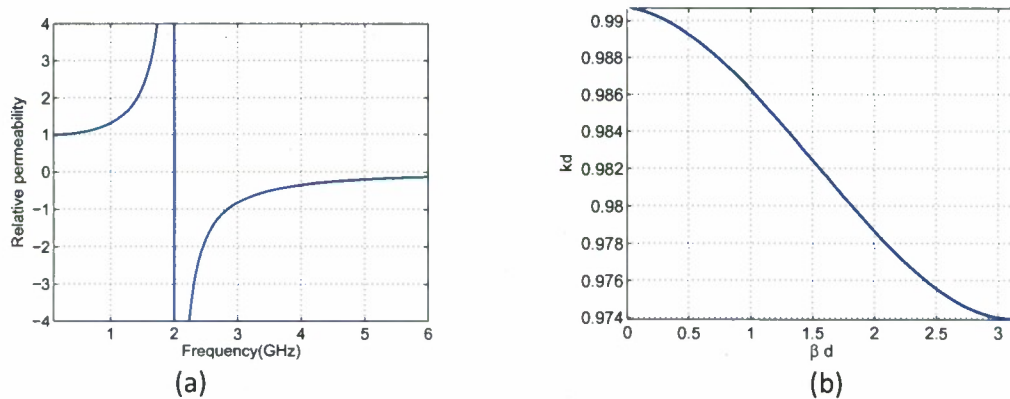


Fig. 12: (a) Plot of the Lorentzian permeability function given by (17). (b) Dispersion diagram characteristic for one-set of dielectric spheres embedded in a Lorentzian host medium with cubical unit-cell and, $a = 0.85 \text{ cm}$, $d = h_x = h_y$, $d/a = 2.1$, $\epsilon_r = 90$.

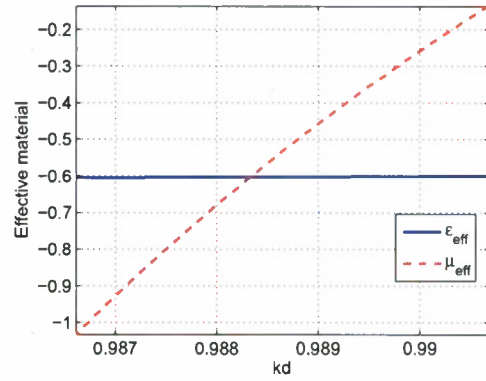


Fig. 13: Effective parameters for a cubical 3D array of dielectric spheres described with, $\epsilon_r = 90$, $a = 0.85 \text{ cm}$, $d/a = 2.1$, inside a negative permeability material with Lorentzian function given by (17). The bulk materials are plotted in the region where both $kd, \beta d < 1$.

4. FDTD Analysis and Other-Shapes Configurations

Although all the results presented so far are for the metamaterials realization by spheres particles, other-shapes particles can also create DNG metamaterials, structures such as disks or rods, achieving the required electric and magnetic dipole modes. Here, the creation of a metamaterial made from array of two types of disks is investigated. Characterization is based on a full wave Finite Difference Time Domain (FDTD) technique.

We will first start with a metamaterial array of dielectric spheres and then we will move to the array of disks. Fig. 14(a) shows the geometry and effective materials parameters for the array of spheres. The FDTD is applied and transmission coefficient is determined in Fig. 14(b). A band-pass region in the DNG band is achieved. The FDTD transmission coefficient result is in great agreement with the dispersion diagram determined by our dipole-mode analysis. The near-fields inside the spheres are shown in Fig. 14(c). It is clearly observed that one set of spheres is equivalent to an electric dipole and the other set equivalent to a magnetic dipole. Combination of these two modes features a backward wave medium.

Fig. 15 illustrates a metamaterial made of array of disks and its characteristics. Electric and magnetic resonances and DNG region are demonstrated. The near-fields are shown in Fig. 16, clearly presents the electric and magnetic modes creation.

A full discussion on FDTD modeling of array of dielectric particles metamaterials along with a comprehensive numerical results and physical understandings have presented in [12].

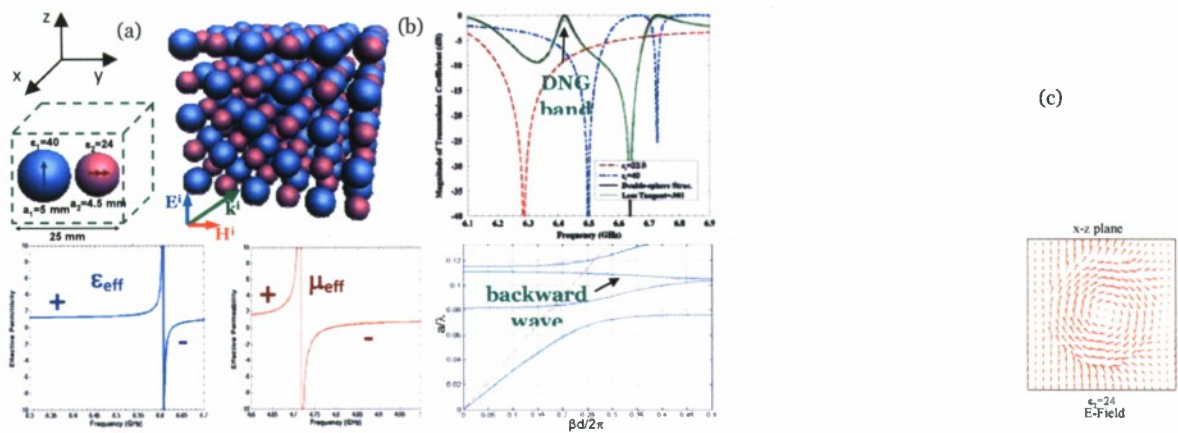


Fig. 14: FDTD analysis for 3D array of spheres providing DNG medium, (a) the geometry, (b) transmission coefficient and dispersion diagram, and (c) near-field patterns.

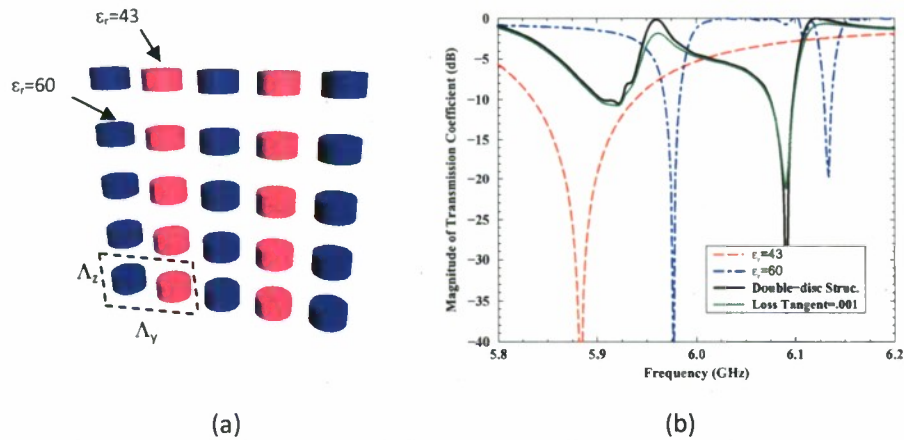


Fig. 15: DNG metamaterial constructed from all-dielectric disks, (a) the geometry ($\Lambda_y = 2.5\text{cm}, \Lambda_z = 1.5\text{cm}$), and (b) its transmission coefficient.

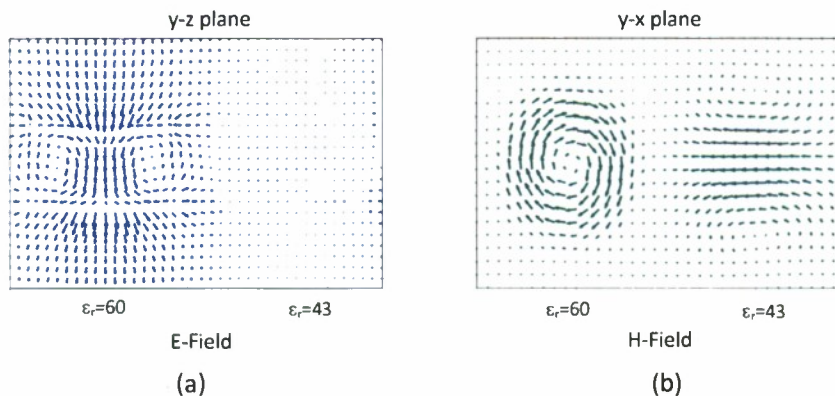


Fig. 16: Field distributions inside one unit-cell of the DNG metamaterial (Fig. 15(a)) at $f = 5.97\text{GHz}$. (a) E in y-z plane, and (b) H in y-x plane. Note to the creation of electric and magnetic dipole moments inside the unit-cell of the disks of $\epsilon_r=60$ and $\epsilon_r=43$.

5. Magneto-Dielectric, ENG, and MNG Spheres Small Antennas

This section explores the performance characterization of small antennas embedded in magneto-dielectric, Epsilon Negative (ENG), and Mu Negative (MNG) spheres. These structures can miniaturize the antennas while at the same time a relatively wide impedance bandwidth can be established. A full detailed-study can be found in [13-17]. Here, we summarize the findings.

5.1 Metamaterials Antennas

Fig. 17 depicts the geometry of an antenna embedded in a hemi-sphere metamaterial located on a ground plane. The resonator of radius a is coupled to a transmission line with a small monopole stub of length l which is located at a distance b from the center of sphere. The objective is to obtain the input impedance of the structure. Using the equivalence principle and image theory one can simply consider the structure as a dipole inside a sphere. Obviously, the input impedance of the original problem is equal to one-half of the new structure.

To obtain the electric field in the z-direction due to the z-directed current element, we first decompose the current vector into the r- and θ -components. Note that r-directed current can only generate TM' modes, where the θ -directed current can generate both TM' and TE' modes. For the θ -directed current, we represent three Green's functions as incident field (dipole only), scattering field inside the sphere (the field inside the sphere caused by the sphere discontinuity), and the scattering field outside the sphere; as given below [13].

$$G_{J_\theta}^{A_i, F_i} = \sum_{n=0}^{\infty} \sum_{m=-n}^n C_{mn}^{A, F} P_n^m(\cos\theta) e^{jm\phi} \begin{cases} \hat{J}_n(kr) & r < r' \\ \hat{H}_n^{(2)}(kr) & r > r' \end{cases} \quad (18a)$$

$$G_{J_\theta}^{A_i, F_i} = \sum_{n=0}^{\infty} \sum_{m=-n}^n D_{mn}^{A, F} P_n^m(\cos\theta) e^{jm\phi} \hat{J}_n(kr) \quad r \leq a \quad (18b)$$

$$G_{J_\theta}^{A_{i_0}, F_{i_0}} = \sum_{n=0}^{\infty} \sum_{m=-n}^n E_{mn}^{A, F} P_n^m(\cos\theta) e^{jm\phi} \hat{H}_n^{(2)}(k_0 r) \quad r \geq a \quad (18c)$$

Where, $\hat{J}_n(x), \hat{H}_n^{(2)}(x), P_n^m(x)$ are spherical harmonics. The unknown coefficients of incident and scattered fields are obtained by applying the boundary conditions. E_θ, E_ϕ and H_θ are continuous, and H_ϕ is discontinuous by θ -directed surface current distributed on $r = r'$ (note that (r', θ', ϕ') refers to source point while (r, θ, ϕ) refers to field point). By matching the boundary condition at $r=a$ the scattering solution for inside and outside are derived.

The next step is to derive the following integral equation for the z-component of electric field:

$$E_z = \iint_{S_0} \left[(\cos\theta G_{J_z'}^{E_i} - \sin\theta G_{J_z'}^{E_\theta}) \cos\theta' - (\cos\theta G_{J_z'}^{E_r} - \sin\theta G_{J_z'}^{E_\phi}) \sin\theta' \right] J_z' dS \quad (19)$$

Where S_0 is the surface on which the current is flowing and J_z' is the z-directed current. Combining the incident field and the scattering field, the z-directed Green's function due to the z-directed current can be written as:

$$\begin{aligned}
G_{\varepsilon_i} = & \frac{-j}{\omega\varepsilon} \left(\frac{\partial^2}{\partial z^2} + k^2 \right) \frac{e^{-jk\sqrt{(z-z')^2 + r_1^2}}}{4\pi\sqrt{(z-z')^2 + r_1^2}} \\
& + \frac{-1}{4\pi\omega\varepsilon k} \frac{\cos\theta\cos\theta'}{r^2 r'^2} \sum_{n=1}^{\infty} n(n+1)h_n P_n(\cos\theta\cos\theta' + \sin\theta\sin\theta'\cos(\phi-\phi')) \hat{y}_n(kr') \hat{y}_n(kr) \\
& + \frac{1}{4\pi\omega\varepsilon} \frac{\sin\theta'\cos\theta}{r^2 r'} \sum_{n=1}^{\infty} h_n \frac{\partial}{\partial\theta'} P_n(\cos\theta\cos\theta' + \sin\theta\sin\theta'\cos(\phi-\phi')) \hat{y}'_n(kr') \hat{y}_n(kr) \\
& + \frac{1}{4\pi\omega\varepsilon} \frac{\cos\theta'\sin\theta}{r r'^2} \sum_{n=1}^{\infty} h_n \frac{\partial}{\partial\theta} P_n(\cos\theta\cos\theta' + \sin\theta\sin\theta'\cos(\phi-\phi')) \hat{y}_n(kr') \hat{y}'_n(kr) \\
& - \frac{k}{4\pi\omega\varepsilon} \frac{1}{r r'} \sum_{n=1}^{\infty} b_n \frac{\partial}{\partial\phi} \frac{\partial}{\partial\phi'} P_n(\cos\theta\cos\theta' + \sin\theta\sin\theta'\cos(\phi-\phi')) \hat{y}_n(kr') \hat{y}_n(kr) \\
& - \frac{k}{4\pi\omega\varepsilon} \frac{\sin\theta'\sin\theta}{r r'} \sum_{n=1}^{\infty} \frac{h_n}{n(n+1)} \frac{\partial}{\partial\theta} \frac{\partial}{\partial\theta'} P_n(\cos\theta\cos\theta' + \sin\theta\sin\theta'\cos(\phi-\phi')) \hat{y}_n(kr') \hat{y}_n(kr) \tag{20}
\end{aligned}$$

where

$$h_n = (2n+1) \frac{\frac{k_0}{\varepsilon_0} \hat{H}_n^{(2)}(ka) \hat{H}_n^{(2)'}(k_0 a) - \frac{k}{\varepsilon} \hat{H}_n^{(2)}(k_0 a) \hat{H}_n^{(2)'}(ka)}{\frac{-k_0}{\varepsilon_0} \hat{H}_n^{(2)'}(k_0 a) \hat{y}_n(ka) + \frac{k}{\varepsilon} \hat{H}_n^{(2)}(k_0 a) \hat{y}'_n(ka)} \tag{21a}$$

$$b_n = \frac{(2n+1)}{n(n+1)} \frac{\frac{k_0}{\mu_0} \hat{H}_n^{(2)}(ka) \hat{H}_n^{(2)'}(k_0 a) - \frac{k}{\mu} \hat{H}_n^{(2)}(k_0 a) \hat{H}_n^{(2)'}(ka)}{\frac{-k_0}{\mu_0} \hat{H}_n^{(2)'}(k_0 a) \hat{y}_n(ka) + \frac{k}{\mu} \hat{H}_n^{(2)}(k_0 a) \hat{y}'_n(ka)} \tag{21b}$$

The method of moment with Galerkin's procedure and Piecewise Sinusoidal (PWS) basis functions are applied to solve for the current. A computer program is developed based on the above equations to successfully characterize the performance of an antenna embedded inside the metamaterial sphere, as will be highlighted next.

The performance of the antenna embedded in dielectric, magneto-dielectric, and ENG hemi-spheres are shown in Figs. 18 and 19. Both ENG and magneto-dielectric metamaterials have better performances compared to only dielectric sphere case. It is shown in [11] that a magneto-dielectric material with both ε and μ parameters can enhance the bandwidth as also explored here (the matching is difficult since a high impedance characteristic is obtained). ENG antenna can successfully miniaturize the antenna size [14-16]. From equation (21a), considering a small dimension for sphere, one can determine

$$\tilde{h}_n = (2n+1) \left(\left(\frac{k_0}{k} \right)^{2n+1} \frac{(n+1)\varepsilon_r + n}{n\varepsilon_r + n+1} - 1 \right) - j \frac{4n}{\sigma\pi k} (n+0.5)!^2 \left(\frac{4}{k^2 a^2} \right)^n \frac{\varepsilon_r - 1}{n\varepsilon_r + n+1} \tag{22}$$

Negative permittivity parameters can make a small antenna resonator as illustrated in Fig. 19. The antenna can resonate at a frequency of interest almost independent of the size, but of course the Q is strongly related to the size [18]. The major issue is that one might not be able to naturally obtain a medium with negative ε in microwave frequencies. Magnetic materials are more promising in this regard as will be explored in next section.

5.2 MNG Antennas

One can use a self-biased hexaferrite in GHz spectrum and operates above the material resonance to provide desired negative permeability [10]. Hence, it will be of practical importance if one can design a small antenna utilizing MNG materials [17]. The system will be dual of ENG antenna, and one needs to excite the structure with a slot excitation realizing magnetic current. Note that, the slot feeding system is more convenient for fabrication than the dipole feed that must be drilled into the ENG medium.

Fig. 20(a) depicts a hemispherical resonator of radius a , composed of a medium with permittivity of ε and permeability of μ , and excited by a slot aperture of length $2l$ and width of W (providing y -directed magnetic dipole). To successfully present a Green's function analysis of the structure, the electromagnetic fields are decomposed into the contributions from the stripline and the slot excitation, and the scattered field due to the sphere discontinuity [17]. Applying the reciprocity theorem along with the assumption that the stripline has an infinite length allow representing the antenna configuration by the following equation:

$$[V_n] = \left\{ [Y_{mn}^o + Y_{mn}^s] + \frac{1}{2} [\Delta v_m] [\Delta v_n]^t \right\}^{-1} [\Delta v_m], \quad (23)$$

where Y_{mn}^s contributes for the effect of the slot, Y_{mn}^o is the admittance caused by the discontinuity of the sphere, and Δv is associated with the slot's discontinuity voltage due to the stripline excitation. Y_{mn}^s is obtained by deriving the Green's function \tilde{G}_{yy}^{HM} , which is the Fourier transform of H_y at $(x,y,0)$ due to a unit \hat{y} -magnetic current located at $(0,0,0)$. It is given by [19]:

$$\tilde{G}_{yy}^{HM} = \frac{-j}{\omega\mu_0} \left[\frac{j(k_1 \cos k_1 d + jk_2 \varepsilon_{rs} \sin k_1 d)(\varepsilon_{rs} k_0^2 - k_y^2)}{k_1 T_m} - \frac{jk_y^2 k_1 (\varepsilon_{rs} - 1)}{T_e T_m} \right] + \frac{(k^2 - k_y^2)}{\omega\mu k_3}, \quad (24)$$

One can determine Δv by deriving the Green's function \tilde{G}_{yx}^{HJ} , which is the Fourier transform of H_y at $(x,y,0)$ due to a unit \hat{x} -electric current element at $(0,0,d)$, it is specified by:

$$\tilde{G}_{yx}^{HJ} = \frac{-jk_x^2 (\varepsilon_{rs} - 1) \sin k_1 d + k_1}{T_e T_m}. \quad (25)$$

The admittance Y_{mn}^o is resulted from the sphere discontinuity and has direct impact on the resonant frequencies. To evaluate it, the Green's function for a y -directed magnetic current located at the center of the sphere should be obtained. It is determined that [17]

$$\begin{aligned} \tilde{G}_{M_y}^{H_{\text{source}}} = \hat{a}_y \left(\frac{-1}{4\pi\omega\mu k} \cdot \frac{\sin\phi \sin\phi'}{r^2 r'^2} \sum_{n=1}^{\infty} n(n+1) b_n P_n(\cos(\phi - \phi')) \hat{J}_n(kr') \hat{J}_n(kr) \right. \\ \left. - \frac{1}{4\pi\omega\mu} \frac{\sin\phi' \cos\phi}{r r'^2} \sum_{n=1}^{\infty} b_n \frac{\partial}{\partial\phi} P_n(\cos(\phi - \phi')) \hat{J}_n(kr') \hat{J}'_n(kr) \right), \end{aligned} \quad (26)$$

where:

$$b_n = (2n+1) \frac{\mu_0}{\mu} \frac{\frac{k_0}{\mu_0} \hat{H}_n^{(2)}(ka) \hat{H}_n^{(2)'}(k_0 a) - \frac{k}{\mu} \hat{H}_n^{(2)}(k_0 a) \hat{H}_n^{(2)'}(ka)}{-\frac{k_0}{\mu_0} \hat{J}_n(ka) \hat{H}_n^{(2)'}(k_0 a) + \frac{k}{\mu} \hat{J}'_n(ka) \hat{H}_n^{(2)}(k_0 a)}. \quad (27)$$

The characteristic equation is then:

$$\Delta_n^{\text{TE}} = \frac{-k_0}{\mu_0} \hat{J}_n(ka) \hat{H}_n^{(2)'}(k_0 a) + \frac{k}{\mu} \hat{J}'_n(ka) \hat{H}_n^{(2)}(k_0 a). \quad (28)$$

For characterizing small size sphere with $ka, k_0a \ll 0.5$ it would be very beneficial if one can obtain an approximated-simple formulation for the Green's function along the slot (y-axis). For this case, one can simplify (approximate) equation (26) as follow:

$$\tilde{G}_{M_r}^{H_{\text{resonant}}} \cong \hat{a}_r \frac{-1}{4\omega\mu k} \sum_{n=1}^{\infty} n(n+1) \tilde{b}_n \frac{1}{(n+0.5)!^2} \left(\frac{k}{2}\right)^{2n+2} (yy')^{n-1}, \quad (29)$$

where

$$\tilde{b}_n = (2n+1) \left(\left(\frac{k_0}{k}\right)^{2n+1} \frac{(n+1)\mu_r + n}{n\mu_r + n+1} - 1 \right) - j \frac{4n}{a\pi k} (n+0.5)!^2 \left(\frac{4}{k^2 a^2}\right)^n \frac{\mu_r - 1}{n\mu_r + n+1}. \quad (30)$$

The resonant frequency of MNG antenna can be predicted from the characteristic equation when $\Delta_n^{\text{TE}} = 0$, where

$$\Delta_n^{\text{TE}} \cong j(k/k_0)^n \frac{k}{(2n+1)\mu} (n\mu_r + n+1), \quad (31)$$

It is observed that the antenna can resonate for $\mu_r = -(n+1)/n$, which is interestingly independent of the sphere size. The first dominant mode ($n=1$) offers resonant frequency at $\mu_r = -2$ (quasi-static model). Higher order modes resonate at other negative permeability values.

Using (24), (25) and (26) (or (29)) one can derive Y_{mn}^s and Y_{mn}^a in an integral equation form depending on the MoM basis functions of the voltage across the slot [20]. The matrix equation (23) can be solved to obtain $[V_n]$, and from that calculate series slot impedance Z_e as:

$$Z_e = Z_c \frac{[\Delta v_n]^t [V_n]}{1 - \frac{1}{2} [\Delta v_n]^t [V_n]}, \quad (32)$$

where Z_c is the characteristic impedance of the stripline. The Z_e is tuned by the open circuit stub length L_s , providing total antenna input impedance:

$$Z_m = Z_e - j \cot(\beta_f L_s), \quad (33)$$

and β_f is the propagation constant in the stripline.

To validate the applicability of the developed formulations, the performance of a MNG hemisphere constructed from a Lorentzian medium is investigated. The hemisphere has radius of $a = 7.5\text{mm}$ and is excited with slot feed having length of $2l = 12\text{mm}$ and width of $W = 0.9\text{mm}$. The Lorentzian permeability function is given by (plotted in Fig. 20(b))

$$\mu = \mu_0 \left(1 - \frac{1}{2} \frac{\omega^2}{\omega^2 - (2\pi \times 2 \times 10^9)^2 - j2\pi \times 4 \times 10^6 \omega} \right) \quad (34)$$

Numerical results for the input impedance based on approximated and exact solutions (equations (29) and (26)) are presented in Fig. 21, verifying the accuracy of the developed formulations. The resonant frequencies are around $f = 2.18\text{GHz}$ and $f = 2.27\text{GHz}$, associated with $\mu_r = -2.09$ (fundamental mode) and $\mu_r = -1.23$ (third mode), respectively. These results successfully validate the applicability of equation (31) in predicting the resonant frequencies. As observed in Fig. 21, the first dominant mode can provide a wider impedance bandwidth. The return loss is shown in Fig. 22, where it demonstrates antenna impedance matching at the first resonant frequency. The -10dB bandwidth is about 0.45%. Tuning the stub length properly matches the antenna at the first resonant frequency. The total size of sphere at the fundamental mode is smaller than $\lambda/9$ ($ka = 0.34$).

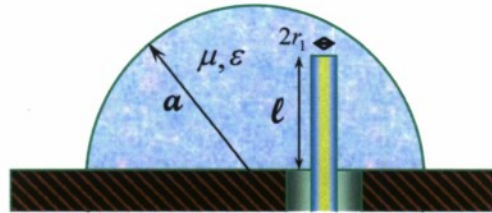


Fig. 17: Configuration of a metamaterial-based antenna.

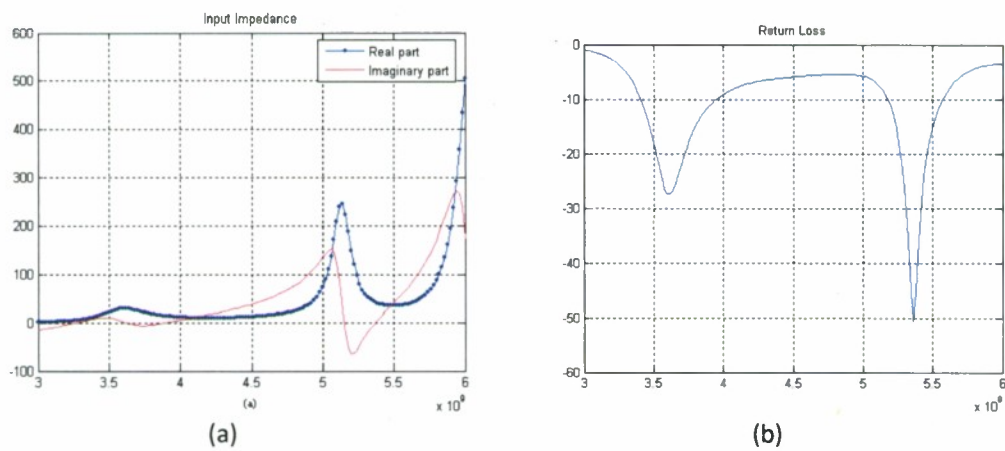


Fig. 18: Input impedance and return loss vs. frequency using delta gap source model. (a) Input impedance. (b) Return loss: $a = 12.5$ mm, $b = 6.4$ mm, $l = 6.5$ mm, $\epsilon_r = 9.8$, $r_1 = 0.063$ mm.

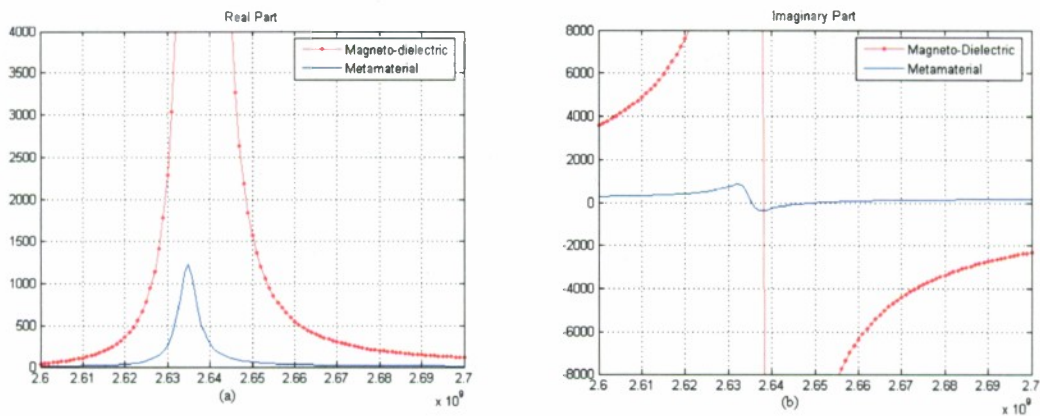
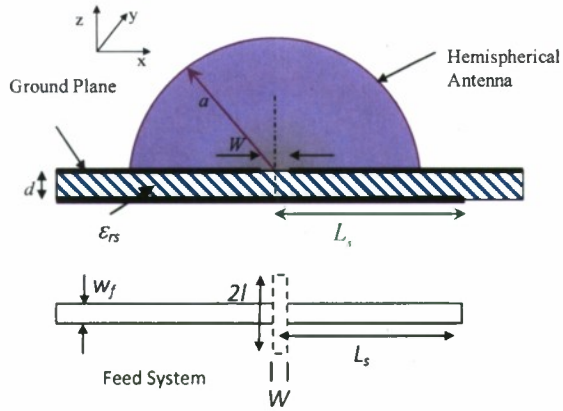
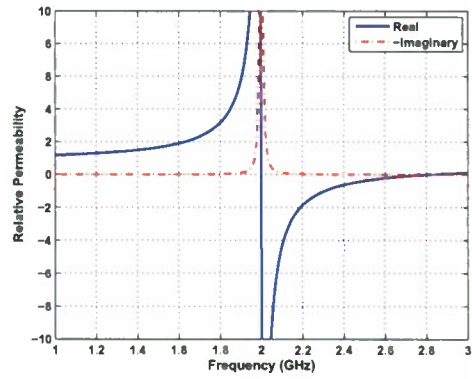


Fig. 19: Input impedance for ENG and magneto-dielectric antennas. (a) Input resistance (b) Input reactance: $a = 7.5$ mm, $b = 0$, $l = 6$ mm, $r_1 = 0.4$ mm. Drude medium with $f_e = 4\text{GHz}$, $\gamma_e = 0.001\omega_e$, and magneto-dielectric material with $(\mu_r = 7.8, \epsilon_r = 6.73)$.

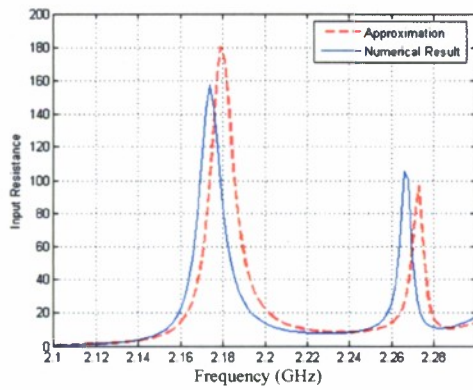


(a)

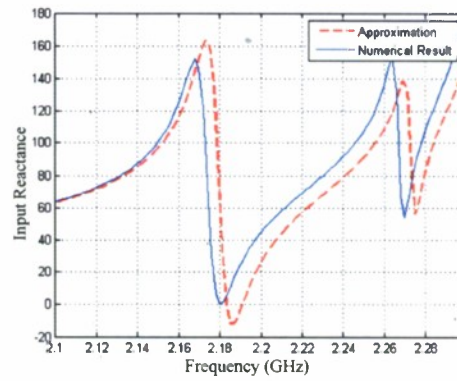


(b)

Fig. 20: (a) The geometry of MNG hemisphere antenna with radius of $a = 7.5\text{mm}$ located above an infinite ground plane, fed by slot with length of $2l = 12\text{mm}$ and width of $W = 0.9\text{mm}$. The stripline has dimensions of $w_f = 1.45\text{mm}$ and $L_s = 2.6\text{cm}$. The substrate has permittivity of $\epsilon_{rs} = 2.96$ and thickness of $d = 0.653\text{mm}$. (b) The plot of Lorentzian permeability function given by (34).



(a)



(b)

Fig. 21: Input impedance of the MNG hemisphere antenna obtained using the approximated and exact Green's functions analysis. (a) Input resistance, and (b) input reactance.

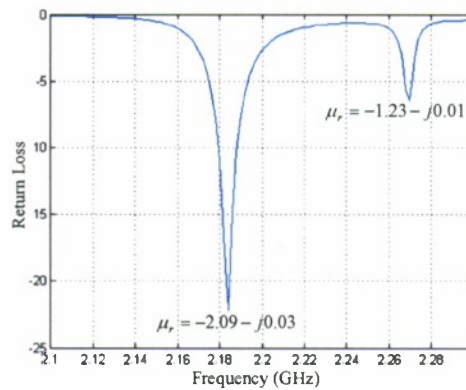


Fig. 22: Return loss of the MNG hemisphere antenna.

References

1. S. Ghadarghadr, *Dipole Mode Analysis of Array of Dielectric and Plasmonic Particles Metamaterials*, PhD thesis, Northeastern University, Boston, MA, to be appeared, 2010.
2. O. R. Cruzan, "Translational addition theorems for spherical vector wave," *Quart. Appl. Math.*, 20, 1962.
3. J. A. Gaunt, On the triplets of helium.
4. Y. L. Xu, "Electromagnetic scattering by an aggregate of spheres," *Applied Optics*, 34, 4573-4588, 1995.
5. Y. L. Xu and B. S. Gustafson, "Experimental and theoretical results of light scattering by aggregates of spheres," *Applied Optics*, 36, 8026-8030, 1997.
6. S. Ghadarghadr and H. Mosallaei, "Dispersion diagram characteristics of periodic array of dielectric and magnetic materials based spheres," *IEEE Trans. Antennas Propagot.*, vol. 57, no. 1, pp. 149-160, Jan. 2009.
7. R. A. Shore and A. D. Yaghjian, *Traveling waves on two- and three-dimensional periodic arrays of lossless acoustic monopoles, electric dipoles, and magnetodielectric spheres*, In House Report, Air Force Research Laboratory, Hanscom, MA, 2006.
8. I. S. Gradshteyn and I. M. Ryzhik. *Table of Integrals, Series and Products*. Academic Press, Boston, 1994.
9. H. Mosallaei, "FDTD-PLRC technique for modeling of anisotropic-dispersive media and metamaterial devices," *IEEE Trans. Electromagn. Comput.*, vol. 49, no. 3, pp. 649-660, Aug. 2007.
10. V. G. Harris, Z. Chen, Y. Chen, S. Yoon, T. Sakai, A. Gieler, A. Yang, Y. He, K. S. Ziemer, N. X. Sun, and C. Vittoria, "Ba-hexaferrite films for next generation microwave devices," *J. Appl. Phys.*, vol. 99, no. 8, paper 08M911, 2006.
11. H. Mosallaei and K. Sarabandi, "Design and modeling of patch antenna printed on magneto-dielectric embedded-circuit metasubstrate," *IEEE Trans. Antennas Propagot.*, vol. 55, no. 1, pp. 45-52, Jan. 2007.
12. A. Ahmadi and H. Mosallaei, "Physical configuration and performance modeling of all-dielectric metamaterials," *Phys. Rev. B*, 77, 045104, 2008.
13. S. Ghadarghadr and H. Mosallaei, "Characterization of metamaterial-based electrically small antennas," *IEEE AP-S International Symposium*, Honolulu, Hawaii, June 10-15, 2007.
14. S. Ghadarghadr and H. Mosallaei, "Electrically small antennas embedded in metamaterials: Closed-form analysis and physical insight," *IEEE AP-S International Symposium*, Honolulu, Hawaii, June 10-15, 2007.
15. A. Ahmadi and H. Mosallaei, "Ellipsoidal negative parameters metamaterial subwavelength radiators," *URSI Notional Radio Science meeting*, Boulder, CO, Jan. 5-8, 2009.
16. H. Mosallaei and S. Ghadarghadr, "Negative material parameters for small antennas design," *URSI Notional Radio Science Meeting*, Ottawa, ON, Canada, July 22-26, 2007.
17. S. Ghadarghadr, A. Ahmadi, and H. Mosallaei, "Negative permeability-based electrically small antennas," *IEEE Antennas and Wireless Propagot. Lett.*, vol. 7, pp. 13-17, 2008.
18. H. R. Stuart and A. Pidwerbetsky, "Electrically small antenna elements using negative permittivity resonators," *IEEE Trans. Antennas Propagot.*, vol. 54, no. 6, pp. 1644-1653, Jun. 2006.
19. D. M. Pozar, "A reciprocity method of analysis for printed slot and slot-coupled microstrip antennas," *IEEE Trans. Antennas Propag.*, vol. 34, no. 6, pp. 1439-1446, Dec. 1986.
20. K. W. Leung, K. M. Luk, K. Y. A. Lai, and D. Lin, "Theory and experiment of an aperture-coupled hemispherical dielectric resonator antenna," *IEEE Trans Antennas Propog.*, vol.43, no. 11, pp. 1192-1198, Nov. 1995.